Reproducibility of protein X-ray diffuse scattering and potential utility for modeling atomic displacement parameters

Zhen Su[1,2], Medhanjali Dasgupta[3], Frédéric Poitevin[1], Irimpan I. Mathews[4], Henry van den Bedem[5,6], Michael E. Wall[7], Chun Hong Yoon[1,a)], and Mark A. Wilson[8,a)]

[1]Linac Coherent Light Source, SLAC National Accelerator Laboratory, Menlo Park, California 94025, USA
[2]Department of Applied Physics, Stanford University, Stanford, California 94305, USA
[3]Molecular Biophysics and Integrated Bioimaging Division, Lawrence Berkeley National Laboratory, Berkeley, California 94720, USA
[4]Stanford Synchrotron Radiation Lightsource, SLAC National Accelerator Laboratory, Menlo Park, California 94025, USA
[5]Bioscience Division, SLAC National Accelerator Laboratory, Menlo Park, California 94025, USA
[6]Department of Bioengineering and Therapeutic Sciences, University of California, San Francisco, California 94158, USA
[7]Computer, Computational, and Statistical Sciences Division, Los Alamos National Laboratory, Los Alamos, New Mexico 87545, USA
[8]Department of Biochemistry and the Redox Biology Center, University of Nebraska, Lincoln, Nebraska 68588, USA

[a)]Authors to whom correspondence should be addressed: yoon82@stanford.edu, mwilson13@unl.edu

Abstract

Protein structure and dynamics can be probed using X-ray crystallography. Whereas the Bragg peaks are only sensitive to the average unit-cell electron density, the signal between the Bragg peaks -- diffuse scattering -- is sensitive to spatial correlations in electron-density variations. Although diffuse scattering contains valuable information about protein dynamics, the diffuse signal is more difficult to isolate from the background compared to the Bragg signal, and the reproducibility of diffuse signal is not yet well understood. Here we present a systematic study of the reproducibility of diffuse scattering from isocyanide hydratase (ICH) in three different protein forms. Both replicate diffuse datasets and datasets obtained from different mutants were similar in pairwise comparisons (Pearson correlation coefficient (CC) ≥0.8). The data were processed in a manner inspired by previously published methods using custom software with modular design, enabling the influence of individual processing steps on data quality to be assessed in a controlled fashion. Using this data processing pipeline, we performed an analysis of data processing choices

to determine which combinations of operations yield the highest quality data as assessed using unbiased measures of symmetry ($CC_{1/2}$) and reproducibility (CC_{Rep}). The diffuse data were then used to characterize atomic mobility using a liquid-like motions (LLM) model of protein motions. Importantly, this characterization was able to discriminate between distinct anisotropic atomic displacement parameter (ADP) models that agreed comparably with the Bragg data. Our results emphasize the importance of data reproducibility as a model-free metric in diffuse data quality evaluation, illustrate the utility of using LLM model analysis to select among alternative ADP models, and offer insights into the design of successful diffuse scattering experiments.

I. INTRODUCTION

In X-ray crystallography, the sharp Bragg reflections are the main source of information for structure determination; however, they only contain information about the average electron density of the unit cell. Diffuse scattering, on the other hand, contains information about the spatial correlations of electron density variations, and thus can, in principle, distinguish between different molecular types of atomic motions that yield the same mean electron density.[1-3] In addition, recent studies suggest that diffuse scattering might be used to extend the resolution of the average electron density beyond the resolution limit of the Bragg peaks,[4,5] motivating further rigorous investigation of this possibility.[6]

Early studies of protein diffuse scattering focused on interpreting features in individual diffraction images.[7-15] Since the development of modern diffuse data processing methods,[16,17] protein diffuse scattering studies have mostly focused on working with three-dimensional (3D) datasets. In addition to improvements in light sources and detectors, notable developments in 3D data processing include finer sampling in reciprocal space to model long-range correlations,[18] rescuing useful diffuse data from experiments designed for Bragg diffraction,[19] extracting finely sampled 3D datasets from serial femtosecond X-ray crystallography (SFX) experiments with X-ray free-electron lasers (XFEL),[4] increasing data quality via improved rejection of the solvent contribution and multivariate analysis methods,[20] and a major advance in the scaling and merging of data from multiple crystals,[21] yielding a substantial improvement in data quality.

Given the variety of approaches to data processing, and the emerging importance of diffuse scattering for modeling protein dynamics, we wished to gain more insight into some fundamental questions about protein diffuse scattering data: How reproducible are single-crystal diffuse datasets? What is the influence of point mutations on the diffuse signal? How do changes in the data translate into differences in a model? What are the consequences of different data processing choices for data quality? Can diffuse scattering data discriminate between different models of atomic mobility that yield similar R_{free}/R_{work} values when refined against the Bragg data?

We address each of these questions in a study of diffuse scattering from crystalline ICH. We selected the ICH system because it diffracts X-rays to atomic resolution at ambient temperature, had clearly visible diffuse features in previous ambient temperature X-ray diffraction datasets, and displays large correlated motion of an α-helix that is modulated by the chemical state of the active site nucleophile.[22] Upon formation of the catalytic thioimidate intermediate, this helix becomes

more mobile and permits water to enter the active site and complete the reaction. Because the extent of this correlated, functionally important α-helix motion can be controlled using various experimental tools, ICH is a valuable system for exploring the utility of diffuse scattering data for characterizing functional protein dynamics.

We also describe an optimized general workflow for the processing and analysis of diffuse data using multiple datasets collected from wild-type (WT) ICH and two mutants (G150A, G150T) that affect helix motion. In addition, we analyze the resulting diffuse scattering data using simple phenomenological models of correlated protein motion: the LLM model[9,11] using three different treatments of ADPs, and a rigid-body translational motions (RBT) model.[1,4] Using multiple replicate datasets and a modular data processing pipeline in Python that we developed, we assessed quantitatively the reproducibility of the data and the influence of various data processing choices on the final quality of the diffuse scattering datasets. Because our processing pipeline is modular in construction, individual steps can be easily modified and their impact on data quality separately evaluated. In this workflow, we assessed the data quality using unbiased measures of the internal consistency ($CC_{1/2}$)[23] and reproducibility (CC_{Rep}), which we compare with prior metrics such as CC_{Laue} and $CC_{Friedel}$. Finally, we determined the impact of these processing choices on the phenomenological models of correlated atomic motion.

Overall, the results of this study indicate that single-crystal diffuse datasets can be measured reproducibly from WT and mutant ICH crystals ($CC_{Rep} \geq 0.81$ to 1.4Å resolution). Differences in diffuse scattering among different ICH mutants are small when assessed directly using the data; however, depending on the method used to obtain crystallographic ADPs, the LLM model yielded substantially different parameter values for the WT compared to the mutant datasets. Importantly, these differences indicate that diffuse scattering can discriminate between ADP models that fit the Bragg data equally well. In addition, the LLM models yield higher correlations with the data than the RBT models. Finally, a systematic investigation of the influence of data processing methods using our Python workflow yielded a matrix of data quality measures, revealing insights into best practices for data collection and processing. In particular, the results emphasize the importance of background subtraction for increasing data quality, and highlight the benefits of adding a step to remove some of the variation in the isotropic radial intensity profiles.[20]

II. METHODS

ICH protein expression and crystallization

WT, G150A, and G150T *Pseudomonas protegens* Pf-5 (formerly *Pseudomonas fluorescens*) ICH proteins were expressed in BL21(DE3) *E. coli*, purified by Ni^{2+}-metal affinity chromatography, and crystallized by hanging drop vapor equilibration as previously described.[22,24] Briefly, ICH crystals were grown at room temperature (~22°C) by mixing 2 µl of protein at 20 mg/ml with 2 µl of reservoir (22-24% PEG 3350, 100 mM Tris-HCl, pH 8.6, 200 mM magnesium chloride and 2 mM dithiothreitol (DTT)) and typically took one week to reach maximum size. Microseeding of drops equilibrated for 6-12 hours improved crystal size and morphology. As previously noted,[22] G150T crystals form in a different space group (C2/I2) than WT and G150A

crystals ($P2_1$) even when seeded with WT crystals. The largest crystals were ~700×700×150 μm, although typically G150A and G150T ICH crystals grew with a more compact prismatic habit than WT ICH.

Diffuse and Bragg X-ray data collection

To study the reproducibility of diffuse scattering in independent samples, data were collected from three crystals of each form of ICH. For simplicity, these datasets are denoted as WT-1, WT-2, WT-3, G150A-1, G150A-2, G150A-3, G150T-1, G150T-2, and G150T-3, indicating the WT, G150A, and G150T mutant ICH proteins. Crystals were mounted in 10 μm thick glass number 50 borosilicate capillaries (Hampton Research) ranging from 0.7 to 1.0 mm diameter and sealed with wax. Excess solution near the crystal was wicked away while retaining a small volume of reservoir solution in the end of the capillary to maintain vapor equilibrium. For WT ICH, the plate-like crystals were mounted "edge-on", such that their shortest axis was roughly parallel to the capillary axis. In this geometry, the X-ray beam illuminates approximately equivalent volumes of the crystal during rotation about the spindle axis, which was parallel with the capillary axis. G150A and G150T ICH crystals had more prismatic habits than WT ICH and did not require special orientation for data collection.

Diffraction data were collected at 274 K on BL12-2 at the Stanford Synchrotron Radiation Lightsource (SSRL) using 16 keV incident X-rays and shutterless data collection with 0.5° rotation/image, 0.3 sec/exposure, and 98% attenuation. The data were recorded on a PILATUS 6M pixel array detector (PAD) with roughly 0.95Å resolution at the edge of the detector for each dataset. Absorbed doses were approximately $2\text{-}4\times10^4$ Gy per crystal as calculated using https://bl831.als.lbl.gov/xtallife.html. Doses were kept low to minimize X-ray-induced oxidation of the catalytic Cys101 nucleophile to sulfenic acid, as has been previously reported.[22,24,25] To allow subtraction of the capillary background scattering from the diffraction images, non-crystal background diffraction patterns were collected using identical parameters to those used for crystal data collection but by increasing the exposure time and slightly shifting the X-ray beam to the region of the capillary away from the crystal, as shown in Fig. 1. The exposure time was 1 second per image for the non-crystal background patterns in order to accumulate more scattered photons and reduce error in the background measurements. The background images were later scaled by the ratio of the exposure times to be equal to the data images.

Analysis of Bragg data

The Bragg data from each crystal were indexed and scaled using XDS,[26] Pointless,[27] and Aimless[28] with statistics reported in Table S1. For G150T, the data were reindexed in I2 in order to have unit cell settings that are similar to those of WT and G150A ICH datasets in space group $P2_1$. Structures of WT, G150A, and G150T ICH were refined against these data in PHENIX (v1.17.1-3660)[29] using riding hydrogen atoms and restrained anisotropic ADPs with weight optimization for coordinate and ADP refinements. Riding hydrogen atoms have their positions calculated from the geometry of the bonded heavier atoms upon which they "ride" and thus

contribute to both the calculation of model structure factors and non-bonded contacts without adding additional refinement parameters. As noted previously[22,24], Ile152 is a Ramchandran outlier in all structures except G150T and is well-supported by the electron density maps in all cases. We also refined protein structures using the Refmac5 package (v5.8.0266)[30] in the CCP4 suite of program[31] in order to compare the behavior of Refmac5- and PHENIX-refined models against the same datasets. The Refmac5 refinements used riding hydrogen atoms and restrained anisotropic ADPs with a matrix weight term of 0.2-0.4. This range for the Refmac5 weight term produced bond length root mean square differences (RMSD) that were comparable to those of the PHENIX-refined models. These refinement protocols produced models with similar R_{free}/R_{work} for the Bragg data (see Table S2 and S3 for refined model statistics). Despite similar R_{free}/R_{work} values, the anisotropic ADPs of the PHENIX-refined models have anisotropy ratios (the ratio of smallest to largest eigenvalues to the ADP variance-covariance matrix) that were lower (more anisotropic) than the Refmac5-refined models (Fig. S1). This difference in anisotropies was observed for all models, but was most pronounced in the WT datasets. Moving from isotropic to anisotropic ADPs decreased the R_{free} value by ~3-4% in all datasets in both Refmac5 (Table S2) and PHENIX (Table S3), confirming that these additional parameters are justified and provide a better model for the Bragg diffraction data than isotropic displacements.

Construction of 3D diffuse scattering maps

Our 3D diffuse map construction pipeline includes six image pre-processing steps followed by 3D merging and two volume processing steps (Fig. 2). The pre-processing steps were designed to convert the raw intensities into useful diffuse signals and to reject non-diffuse intensities such as Bragg peaks, bad pixels, random noise, and isotropic and anisotropic background. In order of application, these steps were: (1) detector masking; (2) bad pixel removal; (3) non-crystal background pattern subtraction; (4) pixel position and intensity corrections; (5) Bragg peak cleaning; and (6) image scaling and radial profile variance removal.[20] Starting with raw diffraction patterns, step (1) was to mask out obvious bad pixels in the detector, including dead pixels, shadows, and grid lines between detector panels, pixels near the beamstop or with intensities that were either non-positive or greater than 10,000 photons. Step (2) was to perform a deeper cleaning of bad pixels, by masking pixels with intensities that are beyond 5 standard deviations from the mean value inside a 11×11 square window. Steps (1) and (2) were also applied to non-crystal background patterns in the same manner. In step (3), the filtered background patterns were scaled by the exposure time and subtracted frame-by-frame from the matching crystal diffraction patterns (see Methods). In step (4), pixel positions were corrected by the parallax broadening effect in the PILATUS 6M detector,[20] and raw pixel intensities were converted to scattering intensities by applying polarization,[16] solid-angle,[16] and detector absorption corrections.[21]

In step (5), Bragg peaks were predicted in positions and further cleaned, although some peaks were already removed in step (2) due to their strong intensities. Pixels were mapped into reciprocal space and converted into fractional Miller indices (h,k,l) using the XDS[26] indexing result. Intensities were identified as belonging to Bragg peaks if their indices (h,k,l) are all within 0.25 to

the nearest integers. The intensity of each Bragg pixel was replaced with the median value in a 11×11 square window centered on this pixel. The order of filtering, background subtraction and correction steps described above is flexible, but Bragg peaks must be cleaned before image scaling and radial profile variance removal in step (6). The diffraction pattern after the previous five steps is considered as a combination of diffuse scattering, random noise and isotropic signals from multiple sources such as the crystal, water and air diffraction. Random noise can be averaged out later in the 3D merging stage, so dealing with the isotropic signal was the main focus in step (6). Firstly, the diffraction pattern was scaled using the radial intensity profile scale factor, calculated by minimizing the L2 distance between radial intensity profiles of the target diffraction pattern and a fixed reference diffraction pattern (the first pattern of each dataset in our method). Another radial profile variance removal step, first described in Peck *et al.*,[20] was applied by performing principal component analysis (PCA) on the matrix of the scaled radial profiles and subtracting the contribution from the subspace of the three largest eigenvalues, as shown in Fig. S2.

Each diffraction pattern corresponds to the intersection of an Ewald sphere surface with the 3D diffraction volume. Diffraction patterns after six pre-processing steps were mapped into reciprocal space using crystal orientations and experiment parameters, including the X-ray wavelength, detector distance (z_d), and pixel size. The orientation information was calculated from XDS[26] indexing results (including the **A** matrix) as well as the relative rotation angles in the experiment. Each pixel located at (x,y,z_d) on the detector corresponds to fractional Miller indices (h,k,l) in reciprocal space, which lies within a voxel in the 3D diffraction volume. The voxel value was measured as the average intensity of all pixels that were assigned to it. To avoid contamination arising from Bragg peaks, we rejected every pixel located within a 0.5×0.5×0.5 box centered on the nearest reciprocal-space point with integer Miller indices. This Bragg rejection step can be equivalently applied in the image pre-processing stage by masking pixels rather than replacing them with median intensities. In previous work, three different methods were mentioned regarding removal of Bragg pixels, by either filtering out Bragg pixels,[16-18] replacing intensities,[32] or preserving Bragg peak intensities together with diffuse scattering features.[21] In this work, we chose to filter out all pixels in Bragg peak positions, as we were interested in large-scale diffuse features that vary on a length scale longer than the separation between Bragg peaks. The other two methods are useful for obtaining more finely sampled datasets and analyzing sharper diffuse scattering features.

The 3D diffraction volume obtained by merging all crystal diffraction patterns (denoted as the raw unsymmetrized map), was symmetrized according to its Laue/Friedel point group into a Laue-/Friedel- symmetrized map. To remove the scattering from other sources such as water, air, and uncorrelated protein motions, the symmetrized map was further processed with an isotropic component subtraction step by subtracting the radially averaged 3D volume to get the symmetrized anisotropic diffuse scattering map (Fig. 2). The 3D anisotropic diffuse scattering map is called the diffuse map in this work, and is assumed to contain anisotropic diffuse scattering features arising from correlated motions in the crystal, although further analysis and modeling are still required to

confirm this. The package for the whole analysis pipeline, including image pre-processing steps, 3D merging, and volume operations, is available online: https://github.com/zhenwork/dspack.

Evaluation of the quality of diffuse scattering maps

The diffuse map produced by our analysis pipeline contains both anisotropic diffuse scattering from correlated protein motions and any merging artifacts that have anisotropic features. Previous studies[16,18,20] have used symmetry metrics such as CC_{Laue} and $CC_{Friedel}$ (see Table 1) to assess the quality of 3D diffuse datasets, calculated using the function,

$$\mathrm{CC}(X,Y) = \frac{\sum_{i=1}^{n}\left(X_i^C - \overline{X^C}\right)\left(Y_i^C - \overline{Y^C}\right)}{\sqrt{\sum_{i=1}^{n}\left(X_i^C - \overline{X^C}\right)^2}\sqrt{\sum_{i=1}^{n}\left(Y_i^C - \overline{Y^C}\right)^2}}, \quad (1)$$

where X^C and Y^C represent two vectors sampled from n common voxels of unsymmetrized (X) and Laue-/Friedel- symmetrized anisotropic maps (Y), respectively, and $\overline{X^C}$ and $\overline{Y^C}$ represent the mean values.

Here, we use two additional metrics for quality evaluation of diffuse maps: the data symmetry ($CC_{1/2}$) and reproducibility (CC_{Rep}). $CC_{1/2}$ is an accepted metric for determining the quality of Bragg diffraction data,[23] and its use for diffuse scattering data was recently reported in the literature.[21] The $CC_{1/2}$ metric was calculated using *phenix.merging_statistics*[29] with the unsymmetrized anisotropic map as input. The $CC_{1/2}$ measures whether the diffuse map follows the target symmetry, but it can be misleading if the diffuse map contains substantial anisotropic background features that partly obey the symmetry. To address this problem, we introduce another metric, CC_{Rep}, which is the average CC between diffuse maps of the selected dataset and other independent datasets measured from different crystals of the same protein (see Table S4). For example, in this work the CC_{Rep} for the first dataset of WT ICH (WT-1) is measured as the average CC of CC(WT-1,WT-2) and CC(WT-1,WT-3), where WT-2 and WT-3 are two additional datasets measured from crystals of WT ICH.

Modeling diffuse scattering data with the LLM model

We applied the LLM model implemented in the Lunus software package,[17] starting with inputs of the experimental Laue-symmetrized diffuse map and the corresponding PDB file refined from Bragg data of the same dataset (Table S2). The LLM model can generate the simulated diffraction volume $I_d(\boldsymbol{q})$ by calculating the function,

$$I_d(\boldsymbol{q}) \propto \left(1 - e^{-q^2\sigma^2}\right)e^{-q^2\sigma^2}\left[I_0(\boldsymbol{q}) * \Gamma_\gamma(\boldsymbol{q})\right], \quad (2)$$

where $I_0(\boldsymbol{q})$ is the squared structure factor of the unperturbed crystal, and $\Gamma_\gamma(\boldsymbol{q})$ is a Fourier transform of atomic displacement correlation function. The LLM model has two refinable parameters: the average atomic displacement σ, which estimates the average amplitude of atomic motions, and the correlation length γ, which is the characteristic length scale of correlated atomic displacements.[9,11] The simulated map was processed with Laue symmetrization and isotropic component subtraction and then compared to the experimental diffuse map. The parameters σ and γ of the LLM model were optimized using the Powell minimization method in scipy.optimize,[33]

using the CC between the model and the data as a target -- the highest value of the correlation is denoted as CC_{LLM}.

For the calculation of $I_0(\boldsymbol{q})$, the LLM model can accept three types of ADPs: zero (one parameter for all atoms), isotropic (one parameter per atom), and anisotropic (six parameters per atom). The isotropic ADPs are calculated as Beq values from the anisotropic ADPs in the input PDB file that were previously refined against the Bragg data. Anisotropic ADPs contain information about both the direction and the amplitude of atomic motion, while the isotropic ADPs contain only information about displacement amplitude. To further examine the utility of using the LLM model for diffuse data analysis, we also fit the diffuse data using the RBT model for comparison, as was performed in a previous study.[34] The RBT model presumes that the only correlated motions are rigid-body translations of asymmetric units and was refined against the diffuse data using the Lunus software.[17] The RBT contains a single fitting parameter σ that describes the average translational displacement of the asymmetric unit. The best-fit correlation of the RBT model to the experimental data, denoted CC_{RBT}, was compared with CC_{LLM} to determine which physical model was in better agreement with the processed diffuse maps.

Determining the importance of various steps in the analysis pipeline

There are several reported methods[4,16,17,20,21,32] for producing 3D protein diffuse scattering datasets, and they differ with respect to image pre-processing, scaling, and radial profile normalization techniques. In this work, we only focused on the most commonly used methods for processing single crystal synchrotron diffuse data[16,17,20,32] as described in Methods, and then studied the effects of non-crystal background subtraction, pixel position and intensity corrections,[16,20,21] radial profile variance removal, and per-image scale factors on the quality and reproducibility of the extracted diffuse scattering maps. We evaluated the impact of each of these processing steps on data quality by sequentially omitting each step in the standard pipeline as well as testing the influence of different scale factors on final data quality. Different processing choices were evaluated using multiple diffuse scattering quality metrics, including $CC_{1/2}$ and CC_{Rep}. A similar type of analysis was used by Meisburger *et al.*[21] to assess different approaches to merged diffuse data using a $CC_{1/2}$ statistic.

For the data processing choice analysis, we capitalized on the modular design of our developed program to turn on, turn off, or tune parameters in specific processing steps. For the present study, choices were assessed by eliminating individual data processing steps and determining the effect on the $CC_{Friedel}$, CC_{Laue}, $CC_{1/2}$, CC_{Rep}, and CC_{LLM} values. In total, we studied seven data processing choices, including (A) the standard pipeline, and processing that omits either (B) the non-crystal background image subtraction, (C) the polarization correction,[16] (D) the radial profile variance removal,[20] (E) the solid-angle correction,[16] (F) the detector absorption correction,[21] or (G) the parallax correction.[20] The values of $CC_{Friedel}$, CC_{Laue}, $CC_{1/2}$, CC_{Rep}, and CC_{LLM} resulting from these processing choices is summarized in Table 2 and Table S5.

To study the effect of choices in the merging approach on data quality, we computed diffraction image scale factors using four different signal sources: (A) the profile of the image

intensity vs. the scattering vector length, (B) the average intensity in the isotropic ring, (C) the average intensity in the diffraction image, and (D) the Bragg peaks. For (A), the profile in each image was scaled to minimize the difference with respect to the profile in a reference image, using intensities within the resolution range (up to 1.4Å). For (B), the scale factor was computed as the ratio of the average pixel intensities within the water ring region (5Å-1.82Å). For (C), the scale factor was computed as the ratio of average pixel intensities within the resolution range. For (D), the Bragg intensity scale factors reported by *dials.scale*[35,36] were used. They are denoted as the (A) radial profile, (B) water ring, (C) overall, and (D) Bragg scale factor, respectively. The standard pipeline in this work uses method (A). The effectiveness of a particular scale factor was evaluated with data quality metrics of the diffuse map processed using that scale factor. The data quality statistics of each scale factor are summarized in Table S6. This table also includes another four choices (E)-(H) where the radial profile variance removal step was turned off as the scale factor was switched from (A) to (D) successively.

III. RESULTS

WT and mutant ICH structures and helix motion

Prior work with ICH showed that X-ray photooxidation of Cys101 results in correlated motion of a helix near the active site that is also observed during formation of the catalytic thioimidate intermediate.[22] These cysteine modification-activated motions in ICH[25] occur owing to transient loss of negative charge on the catalytic cysteine thiolate and facilitate later steps in catalysis. Engineered mutations at residue 150 (e.g. G150A, G150T) also favor shifted conformations of the helix to varying degrees. Because the correlated motion of this helix can be modulated by mutation and the charge of the Cys101 S_γ atom, ICH is an attractive system for exploring diffuse scattering as a probe of functional correlated protein motions.

In this work, structural models refined against replicate Bragg datasets that were collected simultaneously with the diffuse scattering data (see below) are essentially identical (0.02-0.03 Å C_α RMSD). The refined WT and G150A ICH models are also highly similar (~0.05-0.07 Å C_α RMSD). As observed before,[22] the G150T mutation constitutively shifts the helix to the relaxed conformation and crystallizes in a different space group than WT or G150A ICH (see Methods). As expected based on these structural and space group changes, G150T ICH superimposes onto WT and G150A ICH with a larger C_α RMSD of ~0.8 Å (see Fig. 3). In addition, the six WT and G150A datasets show ~2σ difference (mF_o-DF_c) electron density features around the mobile helix that indicate a minor population (>10% occupancy) of the shifted helix conformation. Consistent with our efforts to minimize radiation damage to the crystals, these difference map features are much lower than those observed when Cys101 is oxidized to Cys101-SOH.[22] These minor difference map peaks near the helix could indicate either the basal level of helical mobility in ICH or a response to minor X-ray-induced Cys101 modification in these datasets, possibly including thiyl radical formation.

Quantifying the quality of the experimental diffuse scattering maps

Diffuse intensity is continuously distributed in reciprocal space and is weak compared to Bragg intensity; therefore, robust metrics for quantifying diffuse data quality are needed to avoid the introduction of noise or artifacts into the diffuse maps. Diffraction patterns were processed using our standard pipeline described in Methods to obtain 3D anisotropic diffuse scattering maps for all nine datasets. The diffraction volume was saved in a 3D lattice with 121×121×121 voxels sampled by integer Miller indices. The whole pipeline and visualization of each substep is displayed in Fig. 2. As shown in Fig. 2, anisotropic features were observable in processed diffraction patterns after the removal of Bragg peaks, although they were not as clear as those displayed in 3D diffraction volumes after a deeper noise and isotropic component reduction. The average number of pixels that contribute to the intensity of each non-empty voxel in the diffraction volume is more than 1000 up to 1.4Å, as shown in Fig. S3, leading to a small standard error of the mean. In addition, the isotropic component is more than 10 times stronger than the anisotropic data (Fig. S4). Extracting large-scale anisotropic features from diffuse data therefore is challenging not only due to the high intensity of the Bragg peaks, but also due to the presence of a more intense isotropic component. The Laue-symmetrized anisotropic diffuse maps for all datasets are displayed as section cuts in Fig. 4 and 5 in the q_y and q_z directions, while other visualizations (in the q_x direction) are shown in Fig. S5. Independent datasets of the same protein are very similar, as can be observed from their section cuts. This gives additional confidence that the diffuse maps produced by our pipeline contain *bona fide* protein diffuse scattering data and are not dominated by anisotropic background features or merging artifacts.

In addition to their similarity by visual inspection, we quantified the quality of the extracted diffuse maps using metrics such as percent completeness, $CC_{Friedel}$, and CC_{Laue} (Table 1). The resolution dependent curves of these metrics up to 1.4Å are displayed in Fig. S6. Each dataset is > 95% complete in each resolution shell and > 98% complete over the entire resolution range. The $CC_{Friedel}$ is > 0.7 in each resolution shell and > 0.9 overall. The CC_{Laue} is lower than $CC_{Friedel}$, but it is still > 0.5 in each resolution shell and ≥ 0.85 in the overall resolution range. These numbers have been used to evaluate the data quality of diffuse maps before,[16,18,20] however, in this work we find that the $CC_{Friedel}$ and CC_{Laue} metrics are less sensitive to the data quality than $CC_{1/2}$. For example, $CC_{1/2}$ is roughly twice as sensitive as CC_{Laue} to changes in the diffuse map based on the observed decreases of both metrics in the analysis of different processing choices (Table 2 and S5). In addition, as shown in Table 2, the CC_{Laue} is > 0.75 even without key processing steps such as the polarization correction or radial profile variance removal, where merging artifacts are clearly shown in section cuts of corresponding diffuse maps (Fig. S7 and S8). This suggests that CC_{Laue} fails to evaluate the data quality if there are contaminating background features in the images that roughly obey Friedel or Laue symmetry but are not the desired protein-derived diffuse signal. Based on these findings, we used $CC_{1/2}$ to evaluate internal consistency of a diffuse map in this work, and increased emphasis on reproducibility to assess the data quality.

The $CC_{1/2}$ values for each dataset are provided in Table 1, with the resolution dependent curves shown in Fig. 6. $CC_{1/2}$ varies from 0.76 to 0.89 for all datasets, indicating that the

anisotropic diffuse features obey crystallographic point group symmetry reasonably well. $CC_{1/2}$ is found to increase for the WT-1, WT-3, and G150A-2 datasets when the polarization correction is not used in the diffuse data processing pipeline (C in Table 2). This increase in correlation upon omitting an important correction is caused by the anisotropy in the diffraction pattern introduced by X-ray polarization that does not arise from the sample. Despite not representing crystal-derived diffuse features, these merging artifacts can greatly increase $CC_{1/2}$ values when polarization-induced features happen to coincide with a crystal symmetry axis. As shown in Fig. S7, these polarization features are much stronger along some directions. Importantly, these artifacts are not reproducible between datasets, indicating that inter-dataset reproducibility may be a valuable additional data quality metric for diffuse scattering data.

Because anisotropic background features or artifacts can generate high values for $CC_{1/2}$, another robust and unbiased quality metric for diffuse data is desired. To address this issue, we introduced CC_{Rep} as a measure of the reproducibility of anisotropic diffuse maps of the same protein collected from similar crystals. Collecting multiple datasets for the calculation of CC_{Rep} is not a large experimental burden, as PADs and shutterless data collection have reduced the time needed to collect a complete dataset to a few minutes at most synchrotron beamlines. The inter-dataset metric CC_{Rep} is valuable because it is not expected to be confounded as much as $CC_{1/2}$ by artifacts or background scattering from the mount. Both metrics can be used together to increase confidence in the assessment of the quality of the anisotropic diffuse data. These two metrics also provide means to compare different data processing pipelines and to evaluate the effect of each submodule during processing, as we discuss below.

The CC_{Rep} statistics is summarized in Table 1, with the resolution dependent CC curves of dataset pairs of the same protein shown in Fig. 7. CC_{Rep} is > 0.8 for all datasets processed using the standard pipeline, and drops to lower values when important steps are omitted, as shown in Table 2. The detailed statistics of other diffuse data analysis choices is listed in Table S5. The $CC_{1/2}$ value follows the same trend as CC_{Laue} although it is more sensitive to diffuse data quality, while the CC_{Rep} does not always follow the same trend as $CC_{1/2}$. For example, the data quality of G150A-2 dataset processed without the polarization correction (C in Table 2) shows that, its CC_{Laue} value increases by 0.07, and $CC_{1/2}$ value increases by 0.13 due to the presence of merging artifacts with symmetrical features (Fig. S7). In contrast, CC_{Rep} decreases by 0.31, demonstrating that the improvement in $CC_{1/2}$ might be due to background features or artifacts that are not reproducible in independent samples. Using the standard processing pipeline, all ICH datasets display good $CC_{1/2}$ and CC_{Rep} values.

The near-identical WT and G150A ICH dimeric protein structures (C_α RMSD~0.06 Å) provide an opportunity to evaluate the cross-correlation coefficient (CC_{Cross}) of their diffuse scattering maps. WT and G150A crystallize in the same space group, while G150T crystallizes in a different space group with a related cell to WT and G150A ICH (see Methods). The CC_{Cross} for WT-1, for example, can be calculated as the average CC of CC(WT-1, G150A-1), CC(WT-1, G150A-2), and CC(WT-1, G150A-3). We find that the CC_{Cross} is ≥ 0.83 for every WT and G150A dataset (Table 1), and each data pair within the set of replicate WT and G150A datasets also have

CC ≥ 0.8, as shown in orange colored cells in Table S4. The high cross correlation between WT and G150A diffuse datasets provides additional evidence that protein-derived diffuse scattering is the dominant feature in the processed diffuse anisotropic maps and is consistent with the minor differences in the crystal structures refined against the Bragg data.

Evaluating models of protein motion using the LLM and RBT models

Much of the motivation for collecting diffuse data has been their value in evaluating different models of correlated atomic motions. In this work, we use the LLM and the RBT models as implemented in Lunus[17] (see Methods). These models offer fundamentally different views of correlated atomic motion and were used to determine if internal protein motions make a measurable contribution to the ICH diffuse scattering signal. The LLM model posits that atomic motions in macromolecules have pairwise correlations that decay exponentially with a characteristic length γ.[9] The magnitude of the atomic displacement is given by σ, which is refined as a single value for all of the atoms in the unit cell in our implementation. By contrast, the RBT model requires pure rigid body translation of the asymmetric unit, imposing more highly correlated motions on the atoms composing the protein.

Just as diffraction patterns can be mapped into reciprocal space to build 3D diffraction volumes, simulated diffraction images can be generated using diffraction volumes obtained from either experimental data or a model. This allows a direct visual comparison between the experimental and simulated diffraction patterns in the same orientation. One example is shown in Fig. S9, which compares the LLM model and the experimental data. In producing such a comparison, it is important to process both images in the same manner; for example, in the case of Fig. S9, the minimum pixel value at each radius was subtracted, to emphasize the anisotropic features. Visual inspection of the simulated and experimental diffuse scattering shows agreement in many regions, although the simulated data display more detailed "granular" features, while the experimental data appear more "smeared".

Typically the individual atomic ADPs are set to zero in the standard LLM model.[16,17] We wondered whether using the refined ADPs (either isotropic or anisotropic) from the structural model (entering the model via the squared structure factor $I_0(\boldsymbol{q})$ in Eq. (2)) might provide the LLM with a more detailed and accurate representation of variations in atomic positions in the protein. We evaluated the performance of the LLM model for various ADP treatments to determine how well the diffuse data can discriminate between different models of atomic displacement. With the Refmac5-refined PDB files, the LLM model statistics for all ICH datasets using different ADP treatments are displayed in Fig. 8 and summarized in Table S7, the resolution dependent CC_{LLM} curves are shown in Fig. S10. In the case of the WT-1 dataset, the zero ADP model yields an overall CC_{LLM} of 0.64 to 1.4Å resolution, with a correlation length γ = 6.7Å and an overall atomic displacement σ = 0.32Å. The CC_{LLM} using the isotropic ADP model is only slightly higher (0.66), with a longer correlation length γ = 7.9Å and much smaller atomic displacement σ = 0.0060Å. Because the refined isotropic ADPs account for a significant portion of the amplitude of atomic motion, we expect the σ should decrease in the LLM model (see Discussion). The anisotropic ADP

model yields a value of CC_{LLM} that is comparable to the isotropic LLM (Table S7), despite being a superior model of the Bragg data. The other datasets show that the CC_{LLM} varies within 0.62-0.72 for the various ADP treatments. The highest CC_{LLM} is always achieved in the isotropic ADP LLM model, which varies within 0.65-0.72. The anisotropic ADP LLM model yields higher correlations than the zero ADP LLM model for most datasets, and slightly lower correlations for WT-3, G150A-1, and G150A-2 datasets. The correlation length γ is shortest (~7.1Å) in the zero ADP LLM model and longest (~8.4Å) in the anisotropic ADP model. We observe that the correlation length increases as the ADP model becomes more detailed in most (seven) datasets in this work.

Despite having comparable model statistics and agreement with the Bragg data, the PHENIX- and Refmac5-refined anisotropic ADP models have different distributions of atomic anisotropy (Fig. S1). To determine if diffuse scattering data could discriminate between Bragg models with distinct anisotropies but comparable R_{work} values, we compared LLM models calculated from either the Refmac5- and PHENIX-refined protein models, which are summarized in Table S7 and S8. In general, the CC_{LLM} values are higher for the Refmac5 anisotropic ADP models compared to those refined in PHENIX, and the residual displacements σ are much lower in most of the Refmac5 models (except for the WT-3). The discrepancies between the Refmac5 and PHENIX models are clearest for the three replicate WT datasets, where the PHENIX anisotropic ADP models agree more poorly with the WT diffuse datasets (CC_{LLM} ~ 0.57) than Refmac5-refined models (CC_{LLM} ~ 0.64) and also display higher-than-expected residual atomic displacements (σ ~ 0.14 Å). The discrepancies of CC_{LLM} and σ between two Bragg models are statistically significant compared to their standard deviations of three replicate WT datasets. This is consistent with the deviation in the anisotropy distributions for the WT PHENIX models from the "bell-shaped" distribution centered on ~0.45 that is typically observed in proteins (Fig. S1).[37,38]. In contrast, the Refmac5-refined models have anisotropy distributions that are closer to the average of other proteins, with fewer extreme anisotropy values (Fig. S1). However, the higher residual σ value for the WT-3 dataset indicates that there may be issues that remain in that Refmac5 anisotropic ADP model, or, alternatively, that there may be issues with the WT-3 diffuse data. Considered together, the improved CC_{LLM} and the more normal distribution of anisotropies for the Refmac5-refined models show that diffuse scattering data favor anisotropic ADP models that possess more plausible features even when the Bragg models have similar R_{free}/R_{work} values. The implications of this observation for using diffuse and Bragg data together to refine crystallographic models are discussed below.

Some studies have indicated that independent rigid-body motions of macromolecules are responsible for a significant portion of the diffuse scattering signal.[4,32] To test this, we implemented an RBT model in Lunus[17] to compare to the LLM treatment discussed above. The CC_{RBT} and protein displacement σ values are summarized in Table S9. The CC_{RBT} (~ 0.54) is lower than CC_{LLM} by about 0.1 for all datasets and ADPs treatments. The optimal displacements σ in the RBT are generally similar to those in the zero ADP LLM model. Interestingly, as in the LLM models, using the Refmac5-refined ADP models (Table S9) produces higher CC_{RBT} than the

PHENIX-refined models (Table S10), although their differences are not as large as those for the LLM model.

Studying the effects of various steps in the analysis pipeline

To determine which aspects of the diffuse scattering experiment and subsequent image processing have the greatest impact on final data quality, we systematically omitted each step in our pipeline and evaluated final data quality. Results of this analysis are partially shown in Table 2 and summarized in Table S5. Data quality assessed using $CC_{1/2}$ and CC_{Rep} does not change greatly when the solid-angle, detector absorption, and parallax correction are omitted. In contrast, omitting the non-crystal background subtraction, polarization correction, or radial profile variance removal step significantly degrades the data quality. The omission of non-crystal background subtraction reduces the two quality metrics by 0.02-0.08 for all datasets, with the visualization only changed slightly (Fig. S11). The omission of the polarization correction reduces CC_{Rep} of all datasets by more than 0.1, with $CC_{1/2}$ varying in a less informative way for each dataset. The omission of radial profile variance removal step reduces both quality metrics by 0.01-0.09 for most datasets and decreases a few of them by more than 0.1. The significant effects of these three steps are expected, as they are critical to remove contaminating anisotropic background intensity and to reduce merging artifacts (Fig. S7, S8). In contrast, other processing steps, such as the solid-angle, detector absorption, and parallax correction, only affect the radial intensity distribution in the diffraction pattern but do not introduce angular anisotropies. In addition, the omission of polarization correction increases the $CC_{1/2}$ value because strong anisotropic artifacts (see Fig. S7) that are introduced by X-ray polarization are not removed. In this case, also omitting the solid-angle correction can scale down the contribution of high resolution data to the calculation of correlations, leading to slight improvements for both $CC_{1/2}$ and CC_{Rep} in the overall resolution range.

For the study of four different scale factors, the radial profile, overall, and water ring scale factors follow the same trend and only vary slightly (Fig. S12). However, the Bragg scale factor is significantly different from the other three, especially in the last half of each dataset where it increases more than the others (Fig. S12). This means that the last half of the images will be scaled to a much higher intensity level using the Bragg scale factor. The data quality metrics using each scale factor treatment are summarized in Table S6, where the radial profile variance removal step is turned on for (A)-(D) and turned off for (E)-(H). The radial profile, overall, and water ring scale factors with radial profile variance removal (A)-(D) produce the same $CC_{1/2}$ and CC_{Rep} for all datasets, while the Bragg scale factor performs slightly worse. However, when the radial profile variance removal step is turned off (E)-(H), all four scale factors perform much worse, with the Bragg scale factor treatment producing very poor diffuse maps that are dominated by merging artifacts, as shown in Fig. S13. Interestingly, only the Bragg scale factor (H) has a measurable effect on the CC_{LLM} even though the data quality as quantified by $CC_{1/2}$ and CC_{Rep} significantly decreases for other processing choices (D)-(G).

IV. DISCUSSION

Using multiple quality metrics to produce high quality diffuse scattering maps

Reliably extracting the relatively weak diffuse scattering signal from raw diffraction images is vital for generating useful diffuse scattering maps for downstream applications. Several different metrics for data quality evaluation have been discussed in this article, including $CC_{Friedel}$, CC_{Laue}, and $CC_{1/2}$ for evaluating internal consistency in diffuse datasets, and CC_{Cross} and CC_{Rep} for measuring inter-dataset reproducibility. CC_{Laue} or $CC_{Friedel}$ evaluate whether the diffuse map follows the same symmetry as the crystal but they have behaviors that make them less desirable as data quality metrics. In particular, CC_{Laue} values change by about half as much as $CC_{1/2}$ values when perturbations to the data processing are introduced (Tables S5, S6). Moreover, the value of CC_{Laue} can be rather high even for a diffuse map with obvious merging artifacts (see Fig. S7). This is in part because each voxel in a symmetrized map contains a contribution from the corresponding voxel in the unsymmetrized map, leading to a nonzero correlation even for random datasets. The correlation is highest for low-symmetry Laue groups: in P1, where CC_{Laue} corresponds to $CC_{Friedel}$, the value is about 0.7 for a random dataset. Because of this, we favor $CC_{1/2}$ as a quality metric.

Despite the benefits of using $CC_{1/2}$ to assess data quality, a symmetry measure alone cannot fully describe the data quality of a diffuse map, especially when the map is dominated by anisotropic background features or artifacts which may approximately obey these symmetries. This consideration motivated our use of the metric CC_{Rep} to validate whether the anisotropic diffuse signal originates from protein crystal diffraction. The paucity of data quality metrics that can discriminate between anisotropic diffuse scattering from the sample and from the background is an important reason that different protocols for constructing diffuse maps have been reported.[17,20,32] The combined use of $CC_{1/2}$ and CC_{Rep} provides a more complete picture of data quality than $CC_{1/2}$ alone. They also helped verify the utility of our standard pipeline, and enabled the processing choice analysis in this work. The CC_{Cross} is a special metric that can be used for two proteins with similar structures and unit cell dimensions, such as WT and G150A ICH in our experiment. It may have particular value when comparing changes in diffuse scattering between similar samples that have been subjected to perturbations such as temperature change, mutation, etc.

Effects of each processing step in the diffuse map construction pipeline

Constructing and modeling the 3D diffuse map is the standard method for diffuse scattering analysis, where the general workflow in different versions is similar but details in each substep vary. Benefiting from the introduction of two additional quality metrics, we are able to perform a detailed analysis of the modular processing choices and scale factor tests in our program to evaluate the impact of each processing step on the overall quality of the anisotropic diffuse map (Tables 2, S5, S6). The standard pipeline works very well for all datasets giving $CC_{1/2} \geq 0.76$ and $CC_{Rep} \geq 0.81$. Among all steps, the parallax, solid-angle, and detector absorption correction have small effects on both $CC_{1/2}$ and CC_{Rep}. As they only modulate the radial intensity distribution in the diffraction pattern, they may affect the atomic displacement size σ in the LLM but do not make

a strong impact on the diffuse data quality. In contrast, the non-crystal background subtraction, polarization correction, and radial profile variance removal have stronger effects on the data quality of extracted diffuse maps. The omission of these steps will affect the angular intensity distribution in the diffraction pattern and introduce strong artifacts or anisotropic background features to the diffuse map, and these contaminating features are indistinguishable from the anisotropic diffuse scattering from the protein crystal. While the other steps can be applied during data analysis, the non-crystal background image subtraction requires acquiring these matched background images at the time of data collection. The collection of non-crystal background patterns has not been consistently performed until recently[21] despite its simplicity. When a shadow from the capillary or beamstop is visible it can be manually masked out from the detector image, but other anisotropic noise may not be visible by eye in the single diffraction pattern and thus can accumulate in the 3D diffuse map. We suggest collecting non-crystal background patterns in future experiments with the rotation method. Similarly, for SFX experiments, data quality might be improved by analyzing non-hit patterns and finding suitable background patterns for subtraction. The radial profile variance removal is another important step to avoid introducing merging artifacts in the diffuse map (Fig. S8), because pixel intensities assigned to the same voxel are not in the same level due to the inhomogeneity of radial intensity profiles of diffraction patterns. Anisotropic artifacts are thus introduced and mixed with diffuse scattering features. An alternative[32] to radial profile variance removal is to subtract the radially averaged profile from each diffraction pattern before the 3D merging step, because the difference in image radial profiles is similar to the first principal component. The diffuse map construction pipeline is flexible to some extent and the main focus is to remove anisotropic noise and avoid merging artifacts. Any steps that can affect the angular intensity distribution in the diffraction pattern deserve more attention.

In addition to the processing choice analysis, four different types of per-image scale factors are also evaluated by comparing the data quality of diffuse maps processed by corresponding scale factors. As shown in Results, the radial profile, overall, and water ring scale factors generate similar results according to our data quality metrics, and perform moderately better than the Bragg scale factor which was adopted similarly by Peck *et al.*[20] using scale factors from XDS. When the radial profile variance removal step is turned off, all four scale factors give much worse results than the standard pipeline and also perform differently, although Fig. S12 shows that curves of the radial profile, overall, and water ring scale factors only vary slightly for all datasets. This indicates that data quality of the diffuse map is very sensitive to changes in the scale factor when radial profile variance removal is absent, while the radial profile variance removal step greatly reduces the impact of scale factors. In any case, the Bragg scale factor always behaves worse than the others, which can be inferred from its distinctive curve that differs from the others especially for the last half images of each dataset. The Bragg scale factor increases to higher values than the other three scale factors and this is probably induced by the decrease of Bragg intensities in the last half diffraction patterns. The radial profile scale factor therefore is preferred for extracting high-quality diffuse maps from ICH diffraction images.

Modelling of diffuse maps using the LLM model

In the standard LLM model,[16,17] $I_0(\boldsymbol{q})$ is computed from the crystal structure after setting all of the ADPs to zero. In addition to using zero ADPs, here we considered two alternative approaches where $I_0(\boldsymbol{q})$ was computed using either the full anisotropic ADPs from the crystallographic refinement, or using effective isotropic ADPs calculated from the anisotropic ADPs. Using zero ADPs, the agreement of the LLM models with the data (CC_{LLM} of ~ 0.65), the value of the atomic displacement σ (~ 0.33 Å), and the value of the correlation length γ (~ 7.1 Å) are all comparable to previous studies of other protein crystals using coarse-grained diffuse data.[16,18,34] Using isotropic ADPs, the optimal LLM models yielded slightly higher correlations with the data than using zero ADPs, and the small differences are statistically significant for WT and G150T proteins compared to the standard deviations of three replicate datasets. The CC_{LLM} of 0.72 for G150T-3 is in the high end compared to the correlations reported from some previous work.[16,18,34] The fitted values of σ for this model are very close to zero, indicating that the ADPs from the Bragg analysis are consistent with an optimal LLM model. Although it could be argued that the low value of σ is a natural consequence of including the atomic displacements in the calculation of $I_0(\boldsymbol{q})$, this behavior is by no means guaranteed (see, for example., the anisotropic ADP case in Table S8). However, the fact that including isotropic ADPs in the LLM leads to a low value of σ lends additional support to the validity of using a LLM model to analyze the ICH diffuse data. We consistently found that the refined correlation lengths γ were longer for the isotropic (~ 8.1 Å) and anisotropic ADP models (~ 8.4 Å) than in the zero ADP model for all nine datasets. The dependence of the correlation length on the complexity of the atomic displacement model was unexpected. However, we note that the LLM used here involves only a single correlation length, whereas it is more likely that displacements with multiple correlation lengths contribute to the actual diffuse signal.[11]

Because atomic motions result in the loss of Bragg intensity and increased diffuse scattering, there has been long-standing interest in combining Bragg and diffuse scattering data to improve models of atomic motion in crystal structures.[2,6,39] By using the LLM model with different anisotropic ADP models, we found that diffuse scattering data can discriminate between more and less plausible representations of anisotropic atomic motion, even when these models have similar R_{free}/R_{work} values and thus cannot be distinguished based on Bragg data alone. Both Refmac5- and PHENIX-refined models agree well with the Bragg data, however the PHENIX models consistently refine to lower anisotropy values (corresponding to more anisotropic motion) than the Refmac5 refinements (see Table S2, S3) and have anisotropy distributions that deviate from the "bell-shaped" curve centered on ~0.45 that is typically observed (Fig. S1).[37,38] The origin of these differing behaviors is unclear, although our use of automatic weight refinement in PHENIX might have contributed and may have been addressed in subsequent releases. In addition, we find that when non-trivial residual displacements are observed in the LLM models that use refined ADPs as input, this indicates that the ADPs deserve additional scrutiny. Interestingly, LLM models with anisotropic ADPs have CC_{LLM} values that are comparable to or lower than models using isotropic ADPs. The lack of improvement going from the isotropic to anisotropic ADP model was

unexpected because anisotropic ADPs contain information about both the preferred directions and amplitudes of motion and substantially improve the agreement of the refined models with the Bragg data (see Methods). While there are several lines of future investigation suggested by our results, the ability of diffuse scattering data to discriminate between models of anisotropic atomic motion that are equally consistent with the Bragg data indicates that joint refinement of models against Bragg and diffuse scattering data is promising and could result in more accurate representations of atomic motion in proteins. We note that because ICH exhibits controllable correlated helical motion, it makes an ideal system in which to explore the ability of diffuse scattering data to discriminate between various representations of correlated secondary structure motions in the future.

Recent articles [4,32] have suggested that independent rigid-body motions are responsible for the majority of the diffuse signal in protein X-ray diffraction. For ICH, we found that the LLM model agrees better with the data than the RBT model for all datasets in all ADP models (CC_{LLM} and CC_{RBT} values in Tables S7 and S9). This result indicates that the large-scale diffuse features in ICH are more accurately described using liquid-like rather than rigid-body motions. As the values of γ from the LLM fits are much smaller than the size of the protein, our results suggest that the correlation lengths inherent in the RBT model might be too long. Note that our findings do not exclude the possibility that coupled rigid-body motions are important for modeling the sharper diffuse features in the neighborhood of the Bragg peak.[21]

It is important to interpret data quality metrics (such as $CC_{1/2}$ and CC_{Rep}) and model quality metrics (CC_{LLM}, CC_{RBT}) in their appropriate contexts. Data quality metrics pertain only to the measured signal and are independent of model quality metrics, which quantify agreement between a representation of the data and the measured signal. However, better data processing approaches are expected to result in more accurate models. A prominent example is the development of paired model refinement in concert with $CC_{1/2}$ for processing Bragg data, which uses the model R_{work} and R_{free} values obtained from refinements against datasets processed to different resolution limits in order to determine the maximal resolution at which meaningful signal is present.[23] Although we did not use a full paired refinement-like workflow, we found that the CC_{LLM} values for the refined LLMs were not sensitive to even serious degradation in the quality of the diffuse maps, unlike the data quality metrics $CC_{1/2}$ and CC_{Rep}. For example, CC_{LLM} does not change significantly even when the diffuse data quality is severely reduced, such as in the WT-3 dataset processed without the radial profile variance removal step (D in Table 2). In this case, the data quality as quantified by CC_{Rep} decreases by 0.11 while CC_{LLM} increases by 0.01. Therefore, we do not currently recommend using model CC values as a metric for evaluating diffuse scattering data processing decisions, although this may change with improved models of correlated motions.

Lessons about experimental best practices for the collection of macromolecular diffuse scattering data

Our detailed analysis of the influence of various processing steps on the quality of diffuse maps allows us to draw some lessons about the most important experimental aspects of collecting

diffuse scattering data. The weakness of diffuse scattering compared to Bragg diffraction places a premium on experimental approaches that reduce background scattering,[21] and our results underscore the importance of careful treatment of the background. Because the speed of modern data collection makes collecting multiple datasets straightforward, we suggest collecting non-crystal background images for all diffuse scattering experiments measured with either the rotation or SFX method. There is broad agreement that the sample-derived signal should be maximized by using large crystals and by reducing sources of scattering in the beamline setup. However, the best choice of the sample mount is still debated. In this study, we used thin-walled borosilicate glass capillaries that are expected to have nearly isotropic background scattering. Even if it is not subtracted from the data, this isotropic background signal should not contribute to the anisotropic diffuse scattering component that is analyzed to evaluate models of correlated motion. However, glass scatters X-rays ~10 more than plastics such as kapton,[40] and thus will produce an intrinsically higher background that obscures weak diffuse scattering signals. While most plastic mounts enjoy the advantage of lower scattering, they generate an anisotropic background owing to scattering by partially oriented molecules that compose the plastic. Our work and those of others[20,21] indicate that combining the collection and careful subtraction of background non-crystal images with PCA analysis allows for effective removal of contaminating anisotropic background signals, though we can not correct for the anisotropic capillary absorption of X-rays diffracted by the crystal. This suggests that plastic capillaries with lower scattering may be preferable for diffuse scattering experiments despite their more anisotropic background. An important consideration with plastic capillaries is that the loop that is typically used to support the crystal in these mounts can generate a large anisotropic background signal. Therefore, it is advisable to use a loop that is smaller than the crystal and to aim the X-ray beam into portions of the crystal that are fully outside the loop throughout the entire rotation range. This is important because it is difficult to collect well-matched non-crystal background images that include empty loop scattering for later subtraction from the diffraction images.

Prior diffuse scattering work has used large, well-diffracting crystals with comparable thickness in all three dimensions.[6,16,19,21] Such crystals are advantageous for diffuse scattering because they place comparable volumes of the crystal in the X-ray beam in all orientations during data collection, resulting in images with similar diffraction intensity throughout the dataset. Here, our WT ICH crystals grew with a difficult, plate-shaped habit that required careful mounting in order to orient the short axis of the plate co-linearly with the capillary axis so that the X-ray beam illuminated similar thicknesses of crystal during rotation. Our initial inspection of diffuse data collected from crystals that were not so carefully oriented indicated that the data quality suffered when the X-ray beam illuminated very different thicknesses of the crystal during data collection. We note that rods do not present this problem so long as the long axis of the rod is roughly collinear with the rotation axis, which is their naturally preferred orientation during capillary mounting. Although it is clear that diffuse scattering researchers previously appreciated the importance of crystal size and shape for data quality, crystal morphology should be considered by

experimentalists when planning a diffuse scattering experiment, particularly if plate-shaped crystals are being used.

Our use of the reproducibility metric CC_{Rep} showed that there was a much larger amount of contaminating anisotropic intensity in the WT-3 dataset compared to the other two replicates, which may not have been obvious had we not collected the other two datasets for comparison. The radial profile variance removal approach was able to remove these problematic features and resulted in a usable final dataset that compared well with its replicates after processing based on the quality metrics. However, the LLM model of WT-3 still stands out as an outlier with a much larger σ in the anisotropic ADP model. The absence of comparable contaminating anisotropic features in WT-1 and WT-2 excludes beamline components, detector issues, or other sources that would be common to all three datasets. It is possible that the culprit is contaminating detritus (e.g. lint, a fiber from the wick, etc.) that may have adhered to the crystal used to collect the WT-3 dataset during mounting. This illustrates the sensitivity of diffuse scattering data to minor sources of non-crystalline scattering that make a negligible contribution to the Bragg data and demonstrates the value of collecting multiple datasets.

The intrinsic weakness of diffuse scattering data presents detection challenges that are tempting to solve by increasing the X-ray dose. However, because diffuse scattering data are typically collected from crystals at ambient (i.e. non-cryogenic) temperatures, radiation damage is a major concern. In this regard, the ICH system was especially valuable, as it contains a radiation-sensitive active site cysteine nucleophile (Cys101) that is readily photooxidized to cysteine-sulfenic acid at doses lower than the typically quoted 3×10^5 Gy dose limit for ambient temperature Bragg data collection.[22,41] We did not see strong evidence of Cys101 oxidation in these datasets, although we cannot exclude that some minor oxidation occurred. The minimal radiation damage in these sensitive crystals indicates that PADs, rapid shutterless data collection, and the use of large beams (~100-200 μm) can limit radiation damage and allow the collection of usable diffuse scattering data from moderately radiation-sensitive protein crystals. As in prior work,[19] we collected usable Bragg and diffuse scattering data simultaneously, and it is possible that such combined Bragg/diffuse datasets could be used for the global refinement of macromolecular structure, atomic mobility, and correlated motions in the future.

V. CONCLUSION

In this work, we have developed a data analysis pipeline to extract diffuse scattering features from X-ray diffraction patterns, and tested it with nine datasets of three different ICH protein forms. Detailed studies were performed to validate the effectiveness of this pipeline and demonstrate how each submodule and different analysis variables can affect the data quality of extracted diffuse maps, where we confirmed the significant impacts of non-crystal background pattern subtraction, radial profile variance removal of radial intensity profiles, and various per-image scale factors. We introduced two unbiased and robust metrics ($CC_{1/2}$ and CC_{Rep}) to evaluate the data quality of diffuse maps, and concluded that a single metric alone is less effective in distinguishing between anisotropic features from crystal diffuse scattering and from merging

artifacts or the anisotropic background. We found that diffuse scattering data can discriminate between different models of anisotropic atomic motion that agree with the Bragg data equally well, and favor models with more typical distributions of anisotropy. In a comparison of the LLM and RBT models of protein motions inside the ICH crystal, we discovered that model-experiment correlations with the LLM model are higher compared to those produced by the RBT model, and in the high end among those reported in some other studies[16,18,34] using the same LLM model. In total, our results suggest that the ICH system is a promising candidate for future studies of internal protein dynamics using diffuse X-ray scattering.

SUPPLEMENTARY MATERIAL

See the supplementary material for additional figures and tables.

ACKNOWLEDGMENTS

Z.S. would like to thank Prof. Mike Dunne for his guidance and support, and Prof. James Holton for the discussion on X-ray scattering rates of glasses and plastics. M.A.W. acknowledges support from NIH R01GM139978. H.v.d.B. was supported by NIH R01GM123159, and by a Mercator Fellowship from the Deutsche Forschungsgemeinschaft (LE 1841/5-1). M.E.W. was supported by the Exascale Computing Project (No. 17-SC-20-SC), a collaborative effort of the U.S. Department of Energy Office of Science and the National Nuclear Security Administration, and the University of California Laboratory Fees Research Program (No. LFR-17-476732). Use of the Stanford Synchrotron Radiation Lightsource and Linac Coherent Light Source (LCLS), SLAC National Accelerator Laboratory, is supported by the U.S. Department of Energy, Office of Science, Office of Basic Energy Sciences under Contract No. DE-AC02-76SF00515. The SSRL Structural Molecular Biology Program is supported by the DOE Office of Biological and Environmental Research, and by the National Institutes of Health, National Institute of General Medical Sciences (P30GM133894). The contents of this publication are solely the responsibility of the authors and do not necessarily represent the official views of NIGMS or NIH.

DATA AVAILABILITY

The raw data that support findings in this work are available in website https://proteindiffraction.org, and the data accession codes are: 10.18430/m3.irrmc.5696 (WT-1), 10.18430/m3.irrmc.5695 (WT-2), 10.18430/m3.irrmc.5694 (WT-3), 10.18430/m3.irrmc.5693 (G150A-1), 10.18430/m3.irrmc.5692 (G150A-2), 10.18430/m3.irrmc.5691 (G150A-3), 10.18430/m3.irrmc.5690 (G150T-1), 10.18430/m3.irrmc.5689 (G150T-2), 10.18430/m3.irrmc.5688 (G150T-3), respectively.

REFERENCES

[1]P. B. Moore, "On the relationship between diffraction patterns and motions in macromolecular crystals," Structure **17**, 1307–1315 (2009).

[2]M. E. Wall, P. D. Adams, J. S. Fraser, and N. K. Sauter, "Diffuse x-ray scattering to model protein motions," Structure **22**, 182–184 (2014).

[3]S. P. Meisburger, W. C. Thomas, M. B. Watkins, and N. Ando, "X-ray scattering studies of protein structural dynamics," Chemical reviews **117**, 7615–7672 (2017).

[4]K. Ayyer, O. M. Yefanov, D. Oberthür, S. Roy-Chowdhury, L. Galli, V. Mariani, S. Basu, J. Coe, C. E. Conrad, R. Fromme, *et al*., "Macromolecular diffractive imaging using imperfect crystals," Nature **530**, 202–206 (2016).

[5]A. J. Morgan, K. Ayyer, A. Barty, J. P. Chen, T. Ekeberg, D. Oberthuer, T. A. White, O. Yefanov, and H. N. Chapman, "Ab initio phasing of the diffraction of crystals with translational disorder," Acta Crystallographica Section A: Foundations and Advances **75**, 25–40 (2019).

[6]M. E. Wall, A. M. Wolff, and J. S. Fraser, "Bringing diffuse x-ray scattering into focus," Current opinion in structural biology **50**, 109–116 (2018).

[7]G. Phillips Jr, J. Fillers, and C. Cohen, "Motions of tropomyosin. crystal as metaphor," Biophysical journal **32**, 485–502 (1980).

[8]J. Doucet and J. Benoit, "Molecular dynamics studied by analysis of the x-ray diffuse scattering from lysozyme crystals," Nature **325**, 643–646 (1987).

[9]D. Caspar, J. Clarage, D. Salunke, and M. Clarage, "Liquid-like movements in crystalline insulin," Nature **332**, 659–662 (1988).

[10]I. Glover, G. Harris, J. Helliwell, and D. Moss, "The variety of x-ray diffuse scattering from macromolecular crystals and its respective components," Acta Crystallographica Section B: Structural Science **47**, 960–968 (1991).

[11]J. B. Clarage, M. S. Clarage, W. C. Phillips, R. M. Sweet, and D. L. Caspar, "Correlations of atomic movements in lysozyme crystals," Proteins: Structure, Function, and Bioinformatics **12**, 145–157 (1992).

[12]K. Mizuguchi, A. Kidera, and N. Gō, "Collective motions in proteins investigated by x-ray diffuse scattering," Proteins: Structure, Function, and Bioinformatics **18**, 34–48 (1994).

[13]P. Faure, A. Micu, D. Perahia, J. Doucet, J. C. Smith, and J. Benoit, "Correlated intramolecular motions and diffuse x–ray scattering in lysozyme," Nature structural biology **1**, 124–128 (1994).

[14]J. Pérez, P. Faure, and J.-P. Benoit, "Molecular rigid-body displacements in a tetragonal lysozyme crystal confirmed by x-ray diffuse scattering," Acta Crystallographica Section D: Biological Crystallography **52**, 722–729 (1996).

[15]S. Héry, D. Genest, and J. C. Smith, "X-ray diffuse scattering and rigid-body motion in crystalline lysozyme probed by molecular dynamics simulation," Journal of molecular biology **279**, 303–319 (1998).

[16]M. E. Wall, S. E. Ealick, and S. M. Gruner, "Three-dimensional diffuse x-ray scattering from crystals of staphylococcal nuclease," Proceedings of the National Academy of Sciences **94**, 6180–6184 (1997).

[17]M. E. Wall, "Methods and software for diffuse x-ray scattering from protein crystals," in *Micro and Nano Technologies in Bioanalysis* (Springer, 2009) pp. 269–279.

[18]M. E. Wall, J. B. Clarage, and G. N. Phillips Jr, "Motions of calmodulin characterized using both bragg and diffuse x-ray scattering," Structure **5**, 1599–1612 (1997).

[19]A. H. Van Benschoten, L. Liu, A. Gonzalez, A. S. Brewster, N. K. Sauter, J. S. Fraser, and M. E. Wall, "Measuring and modeling diffuse scattering in protein x-ray crystallography," Proceedings of the National Academy of Sciences **113**, 4069–4074 (2016).

[20]A. Peck, F. Poitevin, and T. J. Lane, "Intermolecular correlations are necessary to explain diffuse scattering from protein crystals," IUCrJ **5**, 211–222 (2018).

[21]S. P. Meisburger, D. A. Case, and N. Ando, "Diffuse x-ray scattering from correlated motions in a protein crystal," Nature communications **11**, 1–13 (2020).

[22]M. Dasgupta, D. Budday, S. H. De Oliveira, P. Madzelan, D. Marchany-Rivera, J. Seravalli, B. Hayes, R. G. Sierra, S. Boutet, M. S. Hunter, *et al*., "Mix-and-inject xfel crystallography reveals gated conformational dynamics during enzyme catalysis," Proceedings of the National Academy of Sciences **116**, 25634–25640 (2019).

[23]P. A. Karplus and K. Diederichs, "Linking crystallographic model and data quality," Science **336**, 1030–1033 (2012).

[24]M. Lakshminarasimhan, P. Madzelan, R. Nan, N. M. Milkovic, and M. A. Wilson, "Evolution of new enzymatic function by structural modulation of cysteine reactivity in pseudomonas fluorescens isocyanide hydratase," Journal of Biological Chemistry **285**, 29651–29661 (2010).

[25]H. Van Den Bedem and M. A. Wilson, "Shining light on cysteine modification: connecting protein conformational dynamics to catalysis and regulation," Journal of synchrotron radiation **26**, 958–966 (2019).

[26]W. Kabsch, "Xds," Acta Crystallographica Section D: Biological Crystallography **66**, 125–132 (2010).

[27]P. Evans, "Scaling and assessment of data quality," Acta Crystallographica Section D: Biological Crystallography **62**, 72–82 (2006).

[28]P. R. Evans and G. N. Murshudov, "How good are my data and what is the resolution?" Acta Crystallographica Section D: Biological Crystallography **69**, 1204–1214 (2013).

[29]P. D. Adams, P. V. Afonine, G. Bunkóczi, V. B. Chen, I. W. Davis, N. Echols, J. J. Headd, L.-W. Hung, G. J. Kapral, R. W. Grosse-Kunstleve, *et al*., "Phenix: a comprehensive python-based system for macromolecular structure solution," Acta Crystallographica Section D: Biological Crystallography **66**, 213–221 (2010).

[30]G. N. Murshudov, P. Skubák, A. A. Lebedev, N. S. Pannu, R. A. Steiner, R. A. Nicholls, M. D. Winn, F. Long, and A. A. Vagin, "Refmac5 for the refinement of macromolecular crystal structures," Acta Crystallographica Section D: Biological Crystallography **67**, 355–367 (2011).

[31]M. D. Winn, C. C. Ballard, K. D. Cowtan, E. J. Dodson, P. Emsley, P. R. Evans, R. M. Keegan, E. B. Krissinel, A. G. Leslie, A. McCoy, *et al*., "Overview of the ccp4 suite and current developments," Acta Crystallographica Section D: Biological Crystallography **67**, 235–242 (2011).

[32]T. De Klijn, A. Schreurs, and L. Kroon-Batenburg, "Rigid-body motion is the main source of diffuse scattering in protein crystallography," IUCrJ **6**, 277–289 (2019).

[33]P. Virtanen, R. Gommers, T. E. Oliphant, M. Haberland, T. Reddy, D. Cournapeau, E. Burovski, P. Peterson, W. Weckesser, J. Bright, *et al*., "Scipy 1.0: fundamental algorithms for scientific computing in python," Nature methods **17**, 261–272 (2020).

[34]D. C. Wych, J. S. Fraser, D. L. Mobley, and M. E. Wall, "Liquid-like and rigid-body motions in molecular-dynamics simulations of a crystalline protein," Structural Dynamics **6**, 064704 (2019).

[35]G. Winter, D. G. Waterman, J. M. Parkhurst, A. S. Brewster, R. J. Gildea, M. Gerstel, L. Fuentes-Montero, M. Vollmar, T. Michels-Clark, I. D. Young, *et al*., "Dials: implementation and evaluation of a new integration package," Acta Crystallographica Section D **74**, 85–97 (2018).

[36]J. Beilsten-Edmands, G. Winter, R. Gildea, J. Parkhurst, D. Waterman, and G. Evans, "Scaling diffraction data in the dials software package: algorithms and new approaches for multi-crystal scaling," Acta Crystallographica Section D: Structural Biology **76** (2020).

[37]E. A. Merritt, "Expanding the model: anisotropic displacement parameters in protein structure refinement," Acta Crystallographica Section D: Biological Crystallography **55**, 1109–1117 (1999).

[38]F. Zucker, P. Champ, and E. A. Merritt, "Validation of crystallographic models containing tls or other descriptions of anisotropy," Acta Crystallographica Section D: Biological Crystallography **66**, 889–900 (2010).

[39]J. B. Clarage and G. N. Phillips Jr, "[21] analysis of diffuse scattering and relation to molecular motion," in *Methods in enzymology*, Vol. 277 (Elsevier, 1997) pp. 407–432.

[40]E. Maslen, A. Fox, and M. O'Keefe, "International Tables for Crystallography, Vol. C, 2nd ed.," Table 6.1.1.4. Dordrecht: Kluwer Academic Publishers. (1999).

[41]E. de la Mora, N. Coquelle, C. S. Bury, M. Rosenthal, J. M. Holton, I. Carmichael, E. F. Garman, M. Burghammer, J.-P. Colletier, and M. Weik, "Radiation damage and dose limits in serial synchrotron crystallography at cryo-and room temperatures," Proceedings of the National Academy of Sciences **117**, 4142–4151 (2020).

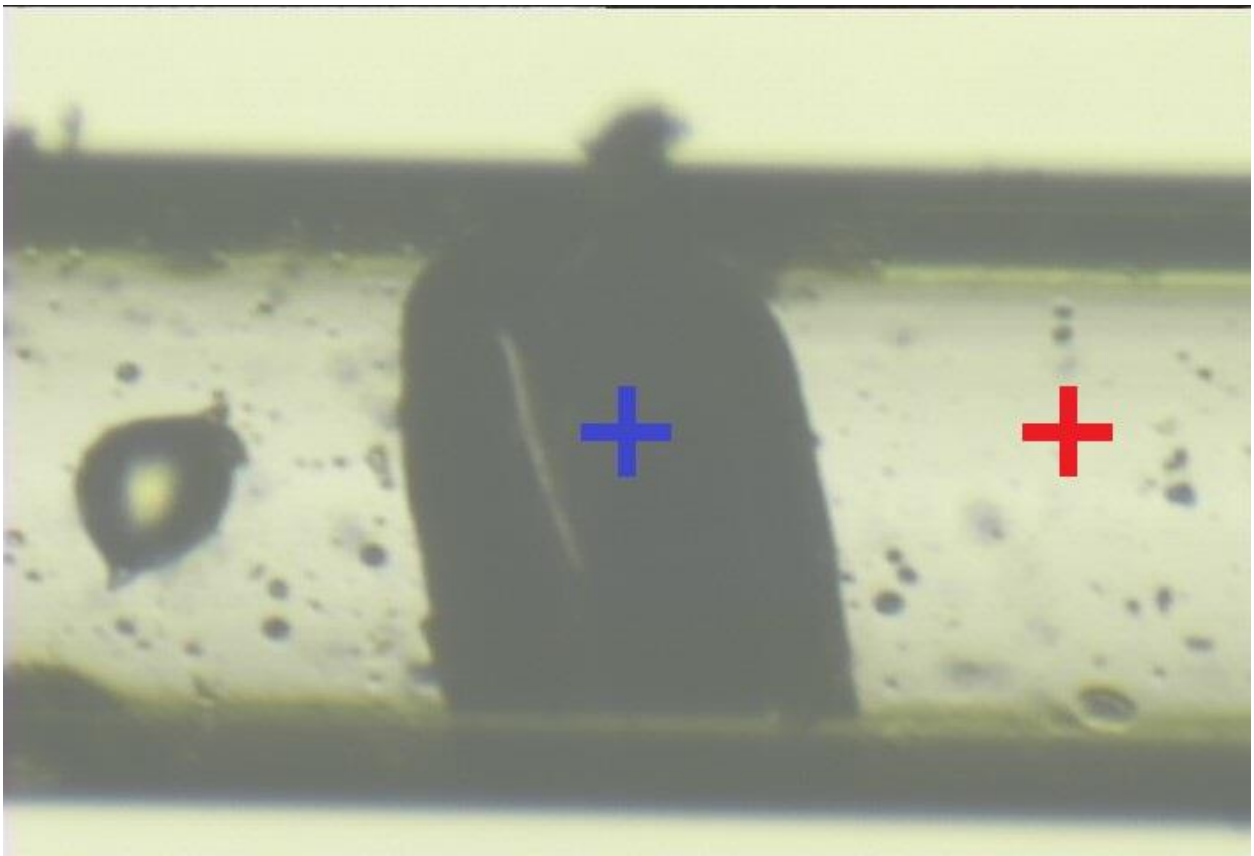

FIG. 1. ICH WT-1 crystal attached to the inside wall of a capillary. The dark object in the center is the WT-1 crystal and the blue cross marks the X-ray beam position for crystal diffraction measurements. The crystal is hydrated by a buffer solution inside the capillary. The non-crystal background images were collected by translating the capillary so that the X-ray beam (red cross) only interacts with the capillary, buffer, and air bubbles. Crystal and background diffraction pattern pairs were collected in each orientation.

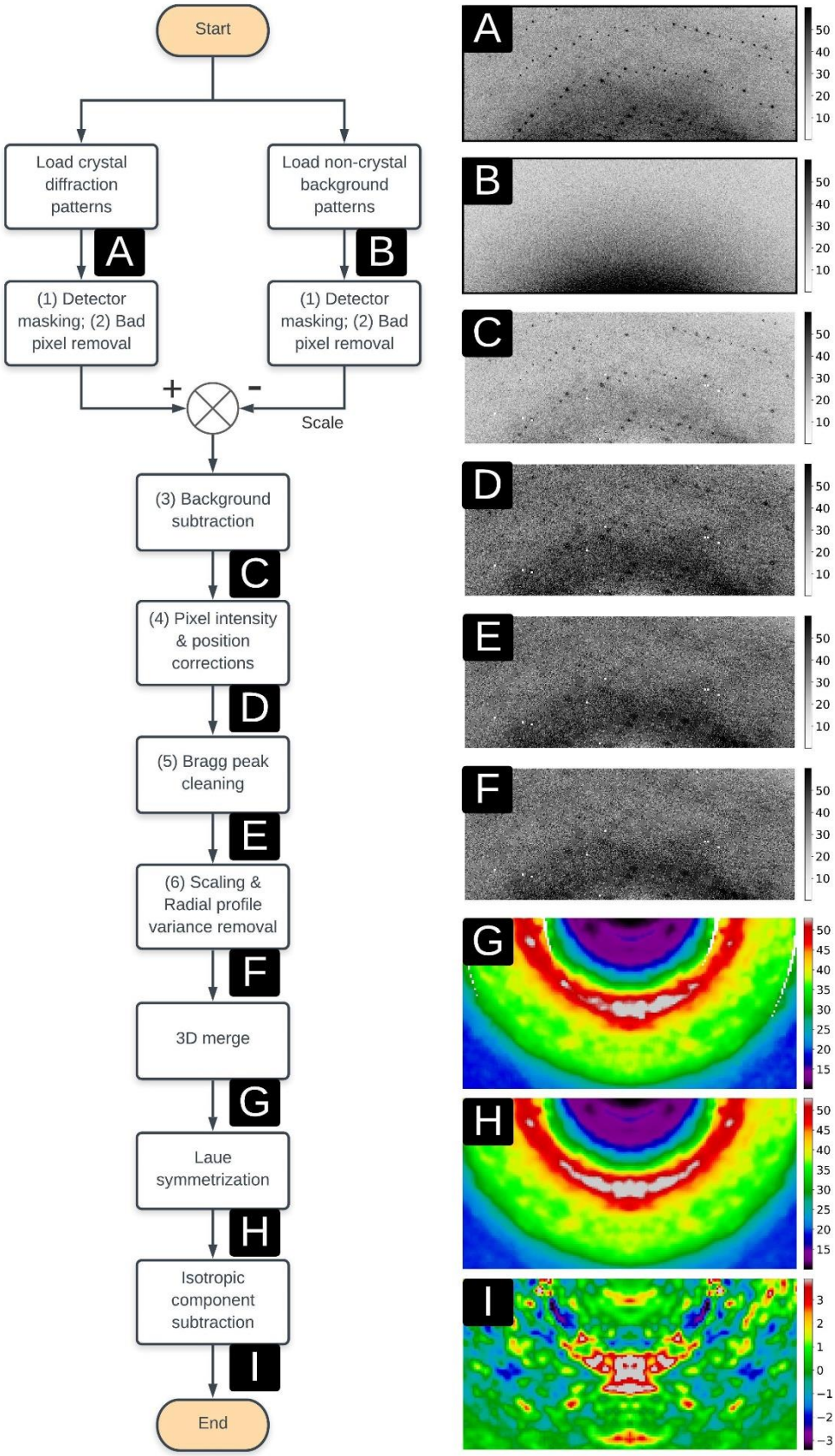
Start
Load crystal diffraction patterns
Load non-crystal background patterns
A
B
(1) Detector masking; (2) Bad pixel removal
(1) Detector masking; (2) Bad pixel removal
+
-
Scale
(3) Background subtraction
C
(4) Pixel intensity & position corrections
D
(5) Bragg peak cleaning
E
(6) Scaling & Radial profile variance removal
F
3D merge
G
Laue symmetrization
H
Isotropic component subtraction
I
End
A
B
C
D
E
F
G
H
I

FIG. 2. Data analysis pipeline from raw diffraction patterns to a Laue-symmetrized anisotropic diffuse map. Numbers (1)-(6) correspond to the same image pre-processing substeps as mentioned in Methods. Following this pipeline, the (A) crystal diffraction and (B) non-crystal background patterns are applied with the user-defined detector mask and a deeper bad pixel removal step based on pixel positions and intensities. The non-crystal background patterns are then scaled with the exposure time and subtracted from crystal diffraction patterns, giving rise to the (C) background subtracted patterns, followed by multiple pixel intensity and position corrections to produce the (D) corrected diffraction patterns. Bragg peaks are predicted in positions and then replaced with median intensities to generate (E) patterns without Bragg peaks, followed by image scaling and the radial profile variance removal method which end up with the final pre-processed diffraction patterns (F). These patterns are merged into a (G) 3D diffraction volume using indexing results and orientations from the goniometer. This 3D volume is then applied with Laue symmetrization to generate the (H) Laue-symmetrized diffraction volume, followed by the isotropic component subtraction step which produces the final (I) Laue-symmetrized anisotropic diffuse map. For improved visualization, panels (G)-(I) were created using more finely sampled diffraction volumes than were used in data quality evaluation and modelling.

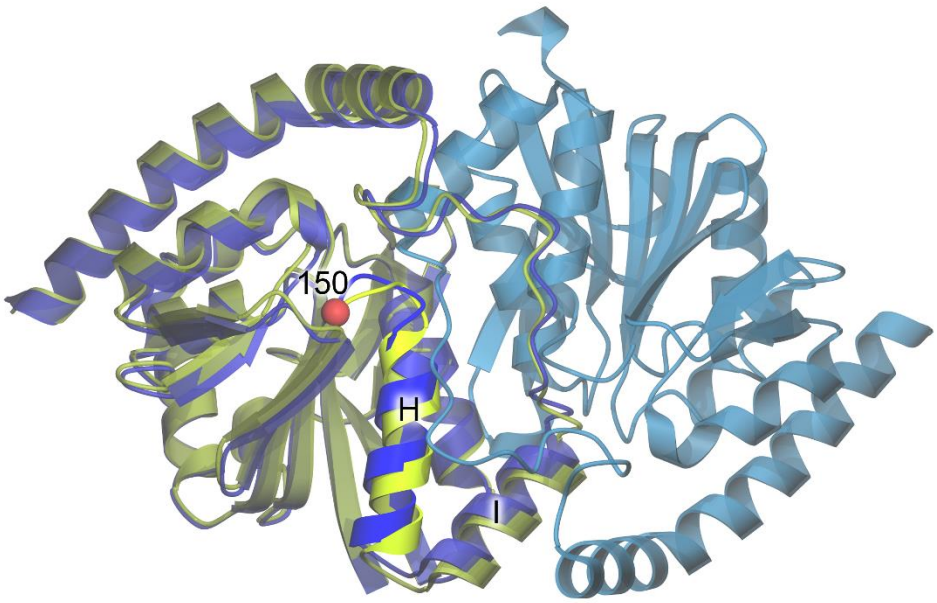

FIG 3. Structure of ICH. The ribbon diagram for the WT ICH dimer is shown in blue, with protomer A colored darker blue and protomer B lighter blue. The structure of G150T ICH (green) is superimposed on protomer A of WT ICH. The location of residue 150 is represented as a red sphere and the mobile helix is labeled H and shown in brighter colors.

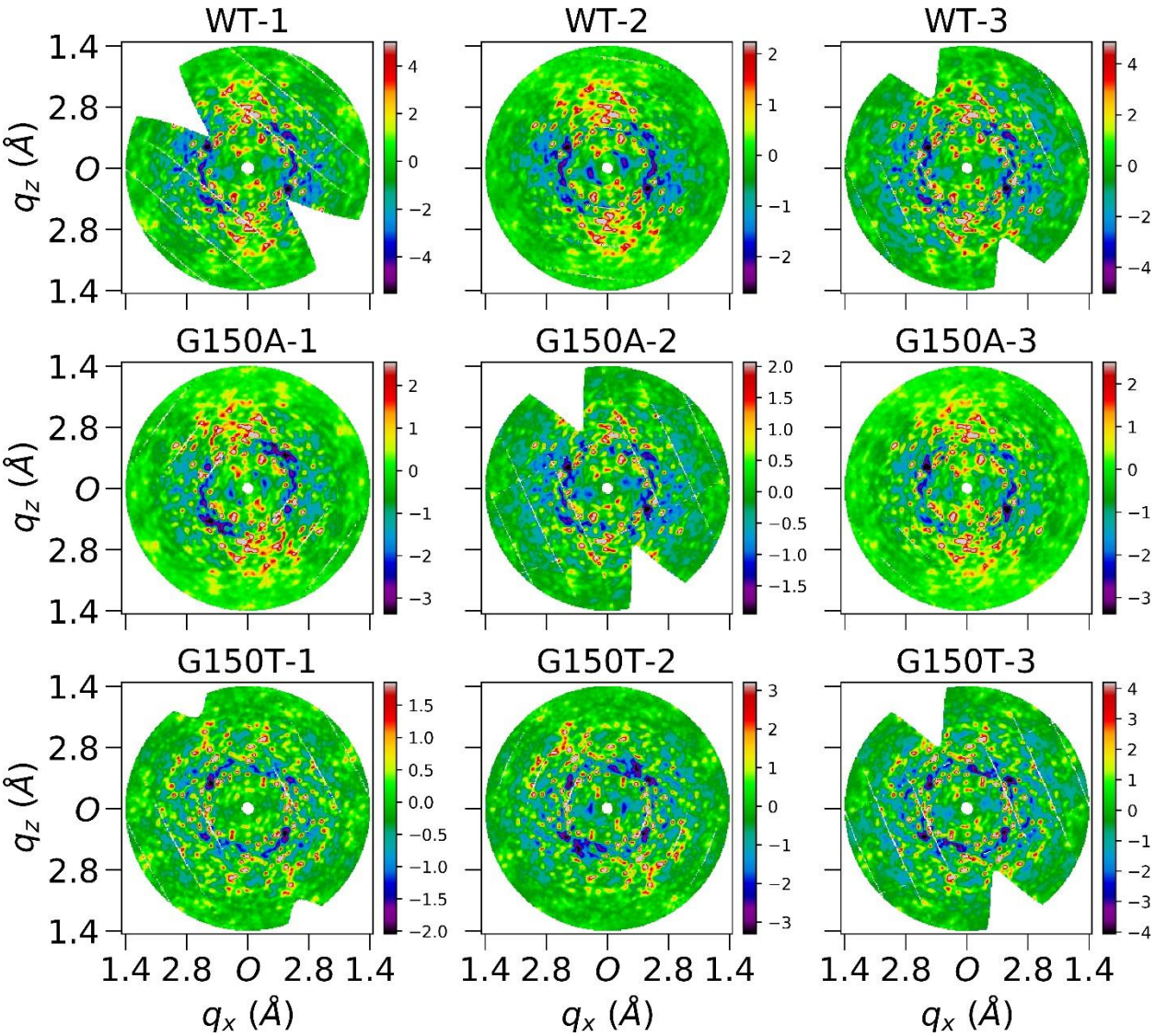

FIG. 4. Central slices of Laue-symmetrized anisotropic diffuse maps (standard pipeline) of nine datasets perpendicular to q_y direction. Each image is cut from the center of the corresponding diffuse map which is three-time finely sampled over Miller indices *H,K,L*. Each subfigure shows average voxels within a depth of 0.05Å^{-1} in q_y direction, and 0.02 × 0.02Å^{-1} in q_xq_z plane. Both q_x and q_z axes extend to 1.4Å, and *O* represents the center in the reciprocal space. These finely sampled diffraction volumes were used for improved visualization only and were not used in data quality evaluation and modelling.

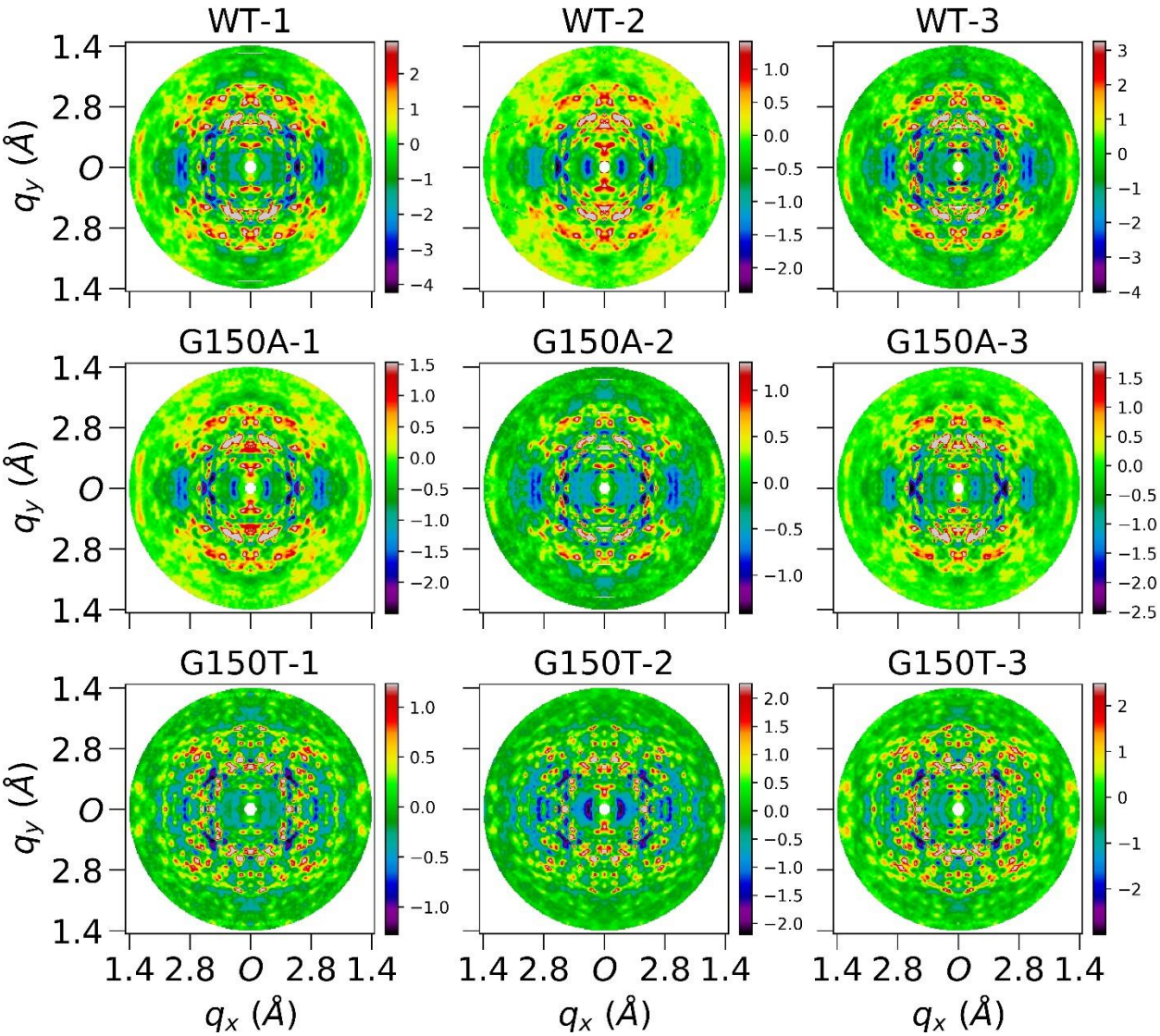

FIG. 5. Central slices of Laue-symmetrized anisotropic diffuse maps (standard pipeline) of nine datasets perpendicular to q_z direction. Each image is cut from the center of the corresponding diffuse map which is three-time finely sampled over Miller indices *H,K,L*. Each subfigure shows average voxels within a depth of 0.05Å^{-1} in q_z direction, and 0.02 × 0.02Å^{-1} in $q_x q_y$ plane. Both q_x and q_y axes extend to 1.4Å, and *O* represents the center in the reciprocal space.

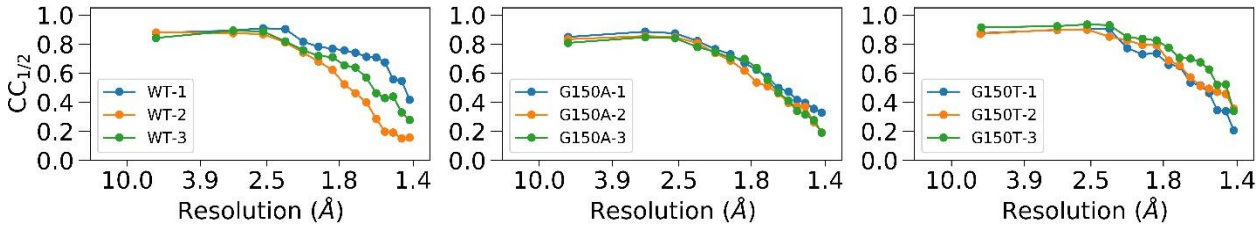

FIG. 6. The resolution dependent $CC_{1/2}$ curves for WT, G150A, and G150T datasets. Each curve was calculated using PHENIX up to 1.4Å, with the unsymmetrized anisotropic map as input.

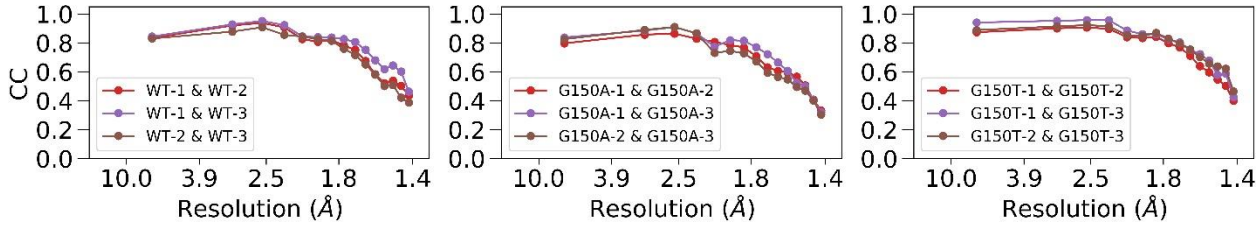

FIG. 7. The resolution dependent CC curves of dataset pairs of the same protein. Each subfigure shows three CC curves between every two independent measurements for WT, G150A, and G150T, respectively. For example, the curve of WT-1 & WT-2 was calculated as the CC between Laue-symmetrized anisotropic diffuse maps of WT-1 and WT-2 datasets.

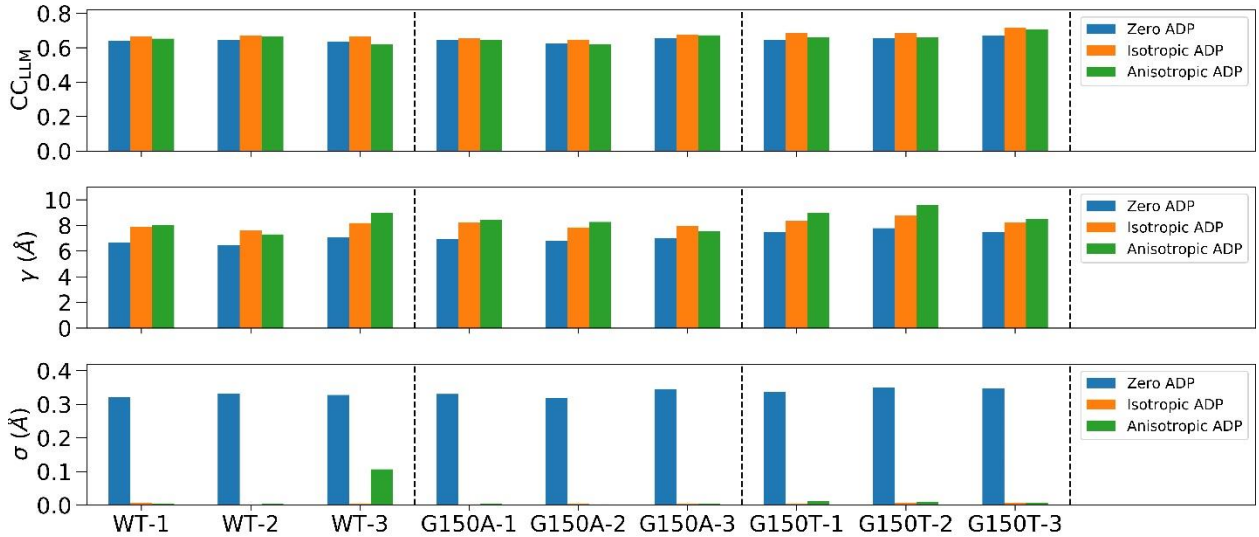

FIG. 8. The LLM model statistics for all ICH datasets using Refmac5-refined PDB files with different ADP treatments. Each subfigure from top to bottom displays the best-fit CC_{LLM}, average correlation length γ, and average atomic displacement σ, respectively. Each dataset was analyzed using three different ADP models including the zero, isotropic, and anisotropic ADP, respectively. The dashed vertical line separates WT, G150A, and G150T datasets.

TABLE 1. The diffuse data quality statistics of each dataset. CC_{Cross} was not evaluated for G150T datasets due to the different space group.

Sample	WT-1	WT-2	WT-3	G150A-1	G150A-2	G150A-3	G150T-1	G150T-2	G150T-3
Compl[1]	98.36	100.0	99.30	100.0	98.80	100.0	99.84	100.0	98.97
$CC_{Friedel}$	0.93	0.91	0.91	0.93	0.91	0.91	0.91	0.92	0.94
CC_{Laue}	0.90	0.87	0.87	0.88	0.86	0.85	0.86	0.88	0.91
$CC_{1/2}$	0.85	0.78	0.81	0.81	0.76	0.77	0.82	0.84	0.89
CC_{Rep}	0.86	0.84	0.85	0.82	0.81	0.82	0.88	0.87	0.89
CC_{Cross}	0.83	0.84	0.85	0.84	0.84	0.85	---	---	---

[1]Compl represents the completeness (%) of the diffuse data.

TABLE 2. The CC statistics of each dataset analyzed with different data processing choices. The diffuse map generated by each processing method was evaluated with 5 CC metrics: $CC_{Friedel}$, CC_{Laue}, $CC_{1/2}$, CC_{Rep}, and CC_{LLM} (anisotropic ADP model). Method A (standard processing pipeline) contains real CC values of each dataset up to 1.4Å, while other methods (B)-(D) are filled with relative CC changes compared to those in method A. Cells in (B)-(D) are colored with 4 different colors depending on the relative changes. A cell is colored as white if the relative CC change is ±0.00, as light blue/red if CC increases/decreases by less than 0.1, otherwise it will be colored as dark blue/red.

Sample	WT-1	WT-2	WT-3	G150A-1	G150A-2	G150A-3	G150T-1	G150T-2	G150T-3
A. Standard data processing pipeline									
$CC_{Friedel}$	0.93	0.91	0.91	0.93	0.91	0.91	0.91	0.92	0.94
CC_{Laue}	0.90	0.87	0.87	0.88	0.86	0.85	0.86	0.88	0.91
$CC_{1/2}$	0.85	0.78	0.81	0.81	0.76	0.77	0.82	0.84	0.89
CC_{Rep}	0.86	0.84	0.85	0.82	0.81	0.82	0.88	0.87	0.89
CC_{LLM}	0.65	0.66	0.62	0.64	0.62	0.67	0.66	0.66	0.71
B. Standard pipeline without non-crystal background image subtraction									
$CC_{Friedel}$	-0.01	-0.01	-0.02	-0.01	-0.03	-0.02	-0.03	-0.02	-0.02
CC_{Laue}	-0.01	-0.03	-0.02	-0.02	-0.03	-0.03	-0.03	-0.04	-0.02
$CC_{1/2}$	-0.02	-0.06	-0.04	-0.04	-0.07	-0.06	-0.06	-0.06	-0.03
CC_{Rep}	-0.03	-0.05	-0.05	-0.08	-0.08	-0.05	-0.03	-0.05	-0.03
CC_{LLM}	-0.00	-0.02	-0.03	-0.03	-0.06	-0.01	-0.04	-0.04	-0.02
C. Standard pipeline without the polarization correction									
$CC_{Friedel}$	+0.04	+0.04	+0.04	+0.03	+0.05	+0.04	+0.03	+0.03	+0.02
CC_{Laue}	+0.05	-0.02	+0.04	-0.01	+0.07	-0.03	+0.03	-0.11	+0.03
$CC_{1/2}$	+0.08	-0.06	+0.08	-0.06	+0.13	-0.11	+0.02	-0.19	+0.04
CC_{Rep}	-0.13	-0.32	-0.27	-0.58	-0.31	-0.32	-0.16	-0.35	-0.15
CC_{LLM}	-0.12	-0.12	-0.25	-0.22	-0.31	-0.13	-0.19	-0.12	-0.21
D. Standard pipeline without the radial profile variance removal step									
$CC_{Friedel}$	-0.01	-0.01	-0.02	-0.02	-0.01	-0.03	-0.02	-0.03	-0.00
CC_{Laue}	-0.02	-0.06	-0.01	-0.05	-0.10	-0.07	-0.03	-0.04	-0.03
$CC_{1/2}$	-0.04	-0.11	-0.03	-0.09	-0.18	-0.15	-0.05	-0.07	-0.04
CC_{Rep}	-0.05	-0.08	-0.11	-0.04	-0.02	-0.04	-0.01	-0.02	-0.01
CC_{LLM}	+0.01	-0.01	+0.01	-0.01	-0.01	-0.05	-0.02	-0.05	-0.02